Supporting Information

$PdSe_2$: Puckered 2D Layers with High Air Stability for Electronics

Akinola D. Oyedele,[†,‡,#] Shize Yang,[⊥,#] Liangbo Liang,[‡,#] Alexander A. Puretzky,[‡] Kai Wang,[‡] Jingjie Zhang,[‡,§] Peng Yu,[ζ] Pushpa R. Pudasaini,[¶] Avik W. Ghosh,[§] Zheng Liu, [ζ] Christopher M. Rouleau,[‡] Bobby G. Sumpter,[‡,∫] Matthew F. Chisholm, [⊥] Wu Zhou, [⊥] Philip D. Rack, [‡,¶] David B. Geohegan,[‡] Kai Xiao[‡,†,*]

[†]Bredesen Center for Interdisciplinary and Graduate Education, University of Tennessee, Knoxville, TN 37996, USA

[‡]Center for Nanophase Materials Sciences, Oak Ridge National Laboratory, Oak Ridge, Tennessee 37831, United States

[⊥]Materials Science and Technology Division, Oak Ridge National Laboratory, Oak Ridge, TN 37830, USA

[§]Department of Electrical and Computer Engineering, University of Virginia, Charlottesville, Virginia 22904, United States

[ζ]Center for Programmable Materials, School of Materials Science & Engineering, Nanyang Technological University, Singapore 639798, Singapore

[¶]Department of Materials Science and Engineering, University of Tennessee, Knoxville, Tennessee 37996, United States

[∫]Computational Sciences & Engineering Division, Oak Ridge National Laboratory, Oak Ridge, Tennessee 37831,

United States

Optical, morphological and device characterization of $PdSe_2$

Morphology and thickness measurements

The morphologies of the $PdSe_2$ flakes were characterized using optical microscopy (Leica DM4500 P) and atomic force microscopy (AFM, Bruker Dimension Icon AFM). The optical contrast being a function of thickness aids the identification of few-layer $PdSe_2$. Thicker samples appear brighter, so monolayer and bilayer $PdSe_2$ areas are more challenging to identify due to their low optical reflectance. Due to tip-surface interaction effects, measuring monolayer flakes can give spurious measurement.[1] For example, monolayer $PdSe_2$ shown in Figure S2 determined by Raman and optical contrast gave a measurement of 3.5 nm. To estimate the thickness accurately, we used the difference in the thickness of corresponding layers, i.e. the difference between 1 L and 2 L, 2 L and 3 L, and so (shown in Figure 2(c)). For accurate measurement, low-frequency Raman[2] was used. This is a subject of ongoing works, results of which will be described in future communications.

Raman and Absorption Spectroscopy

High-resolution Raman measurements were performed using a Jobin-Yvon T64000 spectrometer consisting of a double monochromator coupled to a third monochromator stage with 1800 groves/mm grating equipped with a liquid nitrogen cooled charge-coupled device (CCD) detector. The high-intensity Raman spectra were measured in a custom high optical throughput micro-Raman setup using a 100x microscope objective with NA (numeric aperture) 0.9 (beam spot on the samples was ~1μm). In this case the scattered Raman light was analyzed by a spectrometer (Spectra Pro 2300i, Acton, f=0.3 m) that was coupled to a microscope and equipped with a 1800 groves/mm grating and a CCD camera (Pixis 256BR, Princeton

Instruments). Both high-intensity and high-resolution measurements employed a continuous wave solid-state laser (wavelength 532 nm). All measurements were carried out under a microscope in backscattering geometry.

To measure the absorption spectra of the $PdSe_2$ crystals, a laser-driven light source (EQ-99-fc, Energetiq) was used (spot size at the sample was ~ 2 μm). The transmitted light was captured with a long-distance microscope objective (50×, NA = 0.5) and directed to a spectrometer (Spectra Pro 2300i, Acton) equipped with a CCD camera (Pixis 256BR, Princeton Instruments). All the spectra were collected at room temperature. The absorbance (Abs) was calculated as $Abs = \log_{10}(I_0/I)$, where I and I_0 are the light intensities transmitted through the sapphire substrate on and off a TMD crystal, respectively. Since AFM do not give a precise number of layers, especially for atomically-thin samples, we determine the number of layers, N, from the absorbance, Abs, as $N = Abs/\alpha$, where α is the absorbance per one layer or the absorption coefficient. The absorbance of 30 different crystals versus the number of layers derived from AFM measurements is shown in Figure S7(a) together with its linear fit, that allows one to determine the absorption coefficient, $\alpha=0.0134$, and to find the number of layers based on the absorbance measured at 800 nm (Fig 7b). Figure S7(c) shows the absorption spectra of $PdSe_2$ with various numbers of layers. The Tauc plots, $(ahu)^{1/r}$ versus hv, where $h\upsilon$ is the energy of the incident photons are shown in Fig. 7d. Here, we used $r = 2$, because $PdSe_2$ is an indirect band gap semiconductor.

Field Effect Transistor (FET) Device Characterization

Electrical contacts were fabricated using a combination of electron-beam lithography and evaporation on $PdSe_2$ with different number of layers. Titanium and gold contacts were used for

all the reported devices. Device measurements were done in vacuum, using a probe-up station and a Keithley 4200 semiconductor analyzer. Liquid nitrogen and helium were used for low-temperature characterizations. All devices reported were in two-terminal configuration.

The apparent field-effect mobility was extracted from the linear region of the transfer curve using the equation $\mu_{app} = \left(\frac{L}{WC_{ox}}\right)\left(\frac{\Delta I_{ds}}{\Delta V_{bg}}\right)$, where L is the channel length, W is the channel width, and $C_{ox} = 1.23\times10^{-8} Fcm^{-2}$ is the capacitance between the channel and the back gate per unit area, and taken as $C_{ox} = \varepsilon_0\varepsilon_r / d_{ox}$, where ε_0 = 8.85 x 10^{-12} Fm^{-1}, ε_r = 3.9 and d_{ox} = 280 nm. The term 'apparent' is used because the two-terminal device configuration is limited by contact resistance.

Theoretical Calculations

DFT Calculations

In addition to the functional of optPBE, other functionals implemented in VASP were also tested, including the local density approximation (LDA), PBE, the DFT-D2 approach of Grimme, vdW-DF, vdW-DF2, optB86b-vdW, and optB88-vdW. Overally, the functional of optPBE yields reasonable results for both electronic and structural properties. Starting from the optimized bulk structure, single- and few-layer $PdSe_2$ systems were modeled by a periodic slab geometry with a vacuum region of at least 21 Å in the out-of-plane direction (*z* direction) used to avoid spurious interactions with periodic images. For the 2D slab calculations where 12×12×1 k-point samplings were used, all atoms were relaxed until the residual forces were below 0.001 eV/Å and in-plane lattice constants were optimized using the method of fixing the total volume

(ISIF = 4 in VASP)[3] to avoid the collapse of the vacuum separation in the *z* direction. Our calculations show that the in-plane lattice constants are thickness dependent, owing to the strong interlayer coupling and hybridization in $PdSe_2$. For instance, the loss of the neighboring layers from bulk to monolayer leads to the in-plane lattice shrinking: a is reduced from 5.85 to 5.72 Å, and b reduced from 5.99 to 5.93 Å, according to the optPBE calculations. Few-layer systems also exhibit the in-plane lattice reduction compared to the bulk, but the amplitude of the reduction decreases with the increasing number of layers. Note that the definition of the out-of-plane direction as the *z* direction is in line with the convention of International Crystallography Tables for the bulk, but it is not for *N*L $PdSe_2$. Instead, according to the convention, for odd *N*L $PdSe_2$, the out-of-plane direction should be along the *x* direction; for even *N*L $PdSe_2$, the out-of-plane direction should be along the *y* direction. However, for simplicity and consistency, we chose the *z*-axis as the out-of-plane direction for all thicknesses. As a result, the Raman mode symmetry notations in even *N*L are slightly different from the convention: A_2 and B_1 are swapped. In this work, from bulk to even *N*L, the bulk B_{1g} symmetry is reduced to B_1 instead of A_2.

For the fully relaxed geometries, the dynamic matrix was then calculated using the finite difference scheme implemented in the Phonopy software to obtain phonon frequencies and eigenvectors[4, 5]. Hellmann-Feynman forces in the supercell (2×2×2 for the bulk, while 2×2×1 for single- and few-layer systems) were computed by VASP for both positive and negative atomic displacements (δ = 0.03 Å) and then used in Phonopy to construct the dynamic matrix, whose diagonalization provides phonon frequencies and phonon eigenvectors (i.e., vibrations). Raman scattering calculations were then performed within the Placzek approximation using the in-house developed Raman modeling package. For the j-th phonon mode, Raman intensity is $I \propto \frac{(n_j+1)}{\omega_j}|e_i \cdot \tilde{R} \cdot e_s^T|^2$, where e_i and e_s are the electric polarization vectors of the incident and scattered

lights respectively, and $\tilde{R}$ is the Raman tensor of the phonon mode[6]. ω_j is the frequency of the j-th phonon mode, and $n_j = (e^{\hbar\omega_j/k_BT} - 1)^{-1}$ is its Boltzmann distribution function at the given temperature $T = 300$ K. The matrix element of the (3×3) Raman tensor $\tilde{R}$ of the j-th phonon mode is[6-8]

$$\tilde{R}_{\alpha\beta}(j) = V_0 \sum_{\mu=1}^{N} \sum_{l=1}^{3} \frac{\partial \chi_{\alpha\beta}}{\partial r_l(\mu)} \frac{e_l^j(\mu)}{\sqrt{M_\mu}}, \qquad \text{(S1)}$$

where $\chi_{\alpha\beta} = (\varepsilon_{\alpha\beta} - \delta_{\alpha\beta})/4\pi$ is the electric polarizability tensor related to the dielectric tensor $\varepsilon_{\alpha\beta}$, $r_l(\mu)$ is the position of the μ-th atom along the direction l, $\frac{\partial \chi_{\alpha\beta}}{\partial r_l(\mu)}$ is the derivative of the polarizability tensor (essentially the dielectric tensor) over the atomic displacement, $e_l^j(\mu)$ corresponds to the displacement of the μ-th atom along the direction l in the j-th phonon mode (i.e., the eigenvector of the dynamic matrix), M_μ is the mass of the μ-th atom, and V_0 is the unit cell volume. For both positive and negative atomic displacements (δ = 0.03 Å) in the unit cell, the dielectric tensors $\varepsilon_{\alpha\beta}$ were computed by VASP[9] at the experimental laser frequency 2.33 eV (532 nm) and thus their derivatives were obtained via the finite difference scheme[10]. Based on the phonon frequencies, phonon eigenvectors and the derivatives of dielectric tensors, Raman tensor $\tilde{R}$ of any phonon mode can be obtained. In the experimental back-scattering laser geometry (i.e., the light travels in and out along the z direction, perpendicular to the sample plane), the electric polarization vectors of incoming and scattered light (e_i and e_s) are in the x-y plane. Averaging over all possible in-plane polarizations, the Raman intensity of any given mode in the experimental unpolarized laser configuration is given by $I \propto \frac{1}{4}\frac{(n_j+1)}{\omega_j}|(|\tilde{R}_{11}|^2+|\tilde{R}_{12}|^2+|\tilde{R}_{21}|^2+|\tilde{R}_{22}|^2)$. Finally, based on the calculated Raman intensities $I(j)$ and phonon frequencies ω_j, the Raman spectrum is obtained after Lorentzian broadening.

Optimized bulk $PdSe_2$ structures based on different functionals, pseudopotentials, and DFT softwares

Table S1 lists the optimized bulk $PdSe_2$ lattice constants using different functionals with projector-augmented-wave pseudopotentials in the self-consistent plane-wave DFT package VASP. Among studied functionals, optPBE and optB88 yield the best results compared to the experimental values. Though the structural parameters by optB88 are closer to experimental ones than optPBE, optPBE is found to be better for describing the electronic properties of bulk $PdSe_2$. Compared to optB88 that predicts a negative electronic band gap -0.24 eV (i.e., the energy level of VBM is higher than that of CBM), optPBE yields a much smaller negative band gap -0.02 eV. According to our optical absorption measurements and prior experimental and theoretical works[11-13], bulk $PdSe_2$ has either zero or a very small band gap. Therefore, optPBE seems to be the overall better choice, and it is used for describing the electronic, vibrational and Raman properties of $PdSe_2$ system.

Table S1: Optimized bulk $PdSe_2$ lattice constants using different functionals with projector-augmented-wave (PAW) pseudopotentials in the DFT package of VASP. The experimental values are also shown in the second column for comparison.

Lattice constant	Exp. value	LDA	PBE	DFT-D2	Nonlocal van der Waals functionals				
					vdW-DF	vdW-DF2	optPBE	optB86b	optB88
a(Å)	5.75	6.11	5.79	6.20	5.90	6.01	5.85	6.22	5.85
b(Å)	5.87	6.10	5.94	6.19	6.05	6.15	5.99	6.22	5.97
c(Å)	7.69	6.12	8.48	6.21	8.47	8.34	7.95	6.23	7.63

It is interesting to note that functionals like LDA, DFT-D2 and optB86b yield a completely different structures, where the lattice constants in three directions are nearly the same (around 6.1-6.2 Å). As the lattice in the c direction is decreased, the interlayer distance is shortened and Pd atoms form new bonds with Se atoms in the adjacent layers, and then the originally

orthorhombic layered structure is transformed into the 3D pyrite structure[11, 14]. Such structural transition was investigated previously by external pressure[14]. Because of the existence of two phases in $PdSe_2$, it requires caution for choosing the proper functional for theoretical investigation.

Furthermore, we tested different functionals and pseudopotentials using another DFT software, the self-consistent plane-wave Quantum Espresso[15]. Several vdW functionals with both projector-augmented-wave and norm-conserving pseudopotentials for bulk $PdSe_2$ were considered. The non-local vdW functionals that we considered are vdW-DF, vdW-DF2, C09-DF, C09-DF2, optB86b, optB88 and revB86b[16-18]. For comparison, LDA, PBE and the semi-empirical dispersion correction method DFT-D2 were also considered[19]. The bulk structures were relaxed to a force threshold 1×10^{-3} eV/Å and a pressure threshold 0.5 Kbar with 12×12×10 k-point sampling and 816 eV kinetic energy cutoff. The optimized lattice constants for bulk $PdSe_2$ are listed in Table S2 and Table S3 for different pseudopotentials respectively. Similar to the results by VASP, different functionals and pseudopotentials by Quantum Espresso also yield different structures, including the orthorhombic layered structure and the 3D pyrite structure.

Table S2: Optimized bulk $PdSe_2$ lattice constants using different functionals with projector-augmented-wave (PAW) pseudopotentials in the DFT package of Quantum Espresso.

Lattice constant	LDA	PBE	DFT-D2	Nonlocal van der Waals functionals						
				vdW-DF	vdW-DF2	C09-DF	C09-DF2	optB86b	optB88	revB86b
a(Å)	6.09	5.80	5.79	5.89	6.01	6.16	6.18	5.84	5.86	5.84
b(Å)	6.10	5.95	5.92	6.05	6.16	6.17	6.17	5.95	5.99	5.96
c(Å)	6.10	8.65	7.70	8.68	8.47	6.17	6.19	7.49	7.71	7.53

Table S3: Optimized bulk $PdSe_2$ lattice constants using different functionals with Troullier-Martins type norm-conserving pseudopotentials in Quantum Espresso.

Lattice constant	LDA	PBE	DFT-D2	Nonlocal van der Waals functionals						
				vdW-DF	vdW-DF2	C09-DF	C09-DF2	optB86b	optB88	revB86b
a(Å)	6.10	5.79	5.78	5.90	5.79	6.21	6.22	5.79	5.79	5.79
b(Å)	6.11	5.95	5.92	6.05	5.95	6.22	6.23	5.95	5.95	5.95
c(Å)	6.11	8.72	7.77	8.64	8.68	6.21	6.22	8.68	8.72	8.69 8.69

Discussions

Theoretical Raman calculation

Symmetry assignments of phonon modes for $PdSe_2$ resemble those for black phosphorus. The unit cell of bulk $PdSe_2$ consists of two layers and 12 atoms, and thus there are 36 normal phonon modes at the Γ point whose irreducible representations are:

$$\Gamma_{bulk} = 3A_g + 3B_{1g} + 3B_{2g} + 3B_{3g} + 6A_u + 6B_{1u} + 6B_{2u} + 6B_{3u}, \qquad (S2)$$

where $3A_g$, $3B_{1g}$, $3B_{2g}$ and $3B_{3g}$ modes are Raman active. Raman intensity of a phonon mode is proportional to $|e_i \cdot \tilde{R} \cdot e_s^T|^2$, where e_i and e_s are the electric polarization vectors of the incident and scattered lights respectively, and $\tilde{R}$ is the Raman tensor of the phonon mode[20]. It can be observed by Raman spectroscopy when $|e_i \cdot \tilde{R} \cdot e_s^T|^2$ is not zero. For bulk $PdSe_2$, with the out-of-plane direction defined along the lattice c (i.e., the *z* axis) based on the convention of International Tables for Crystallography, the calculated Raman tensors $\tilde{R}$ of Raman-active modes A_g, B_{1g}, B_{2g} and B_{3g} are

$$\tilde{R}(A_g) = \begin{pmatrix} a & \cdot & \cdot \\ \cdot & b & \cdot \\ \cdot & \cdot & c \end{pmatrix}, \qquad \tilde{R}(B_{1g}) = \begin{pmatrix} \cdot & d & \cdot \\ d & \cdot & \cdot \\ \cdot & \cdot & \cdot \end{pmatrix},$$

$$\tilde{R}(B_{2g}) = \begin{pmatrix} \cdot & \cdot & e \\ \cdot & \cdot & \cdot \\ e & \cdot & \cdot \end{pmatrix}, \qquad \tilde{R}(B_{3g}) = \begin{pmatrix} \cdot & \cdot & \cdot \\ \cdot & \cdot & f \\ \cdot & f & \cdot \end{pmatrix}, \qquad \text{(S3) [Ref 10]}$$

where *a*-*f* are major terms while other terms (denoted by "·") are either zero or negligible due to symmetry. Note that the calculated Raman tensors can also be qualitatively predicted by group theory analysis (see "Bilbao Crystallographic Server")[21, 22]. Raman-inactive modes have zero Raman tensors, thus always zero Raman intensities. Raman-active modes can also have zero intensities, depending on the laser polarizations. In the experimental back-scattering configuration, the electric polarization e_i and e_s are in-plane (the *x*-*y* plane), and thus only Raman modes with non-zero Raman tensor elements $\tilde{R}_{11}$, $\tilde{R}_{12}$, $\tilde{R}_{21}$, or $\tilde{R}_{22}$ can show non-zero intensities. It follows that only A_g and B_{1g} modes can be observed by our unpolarized Raman measurements. This is confirmed by both experimental and theoretical Raman spectra shown in Figure 4(a) and 4(b) in the main text, where the bulk spectra (gray lines) exhibit five peaks. The bulk $PdSe_2$ has 3 A_g modes (A_g^1, A_g^2, A_g^3) and 3 B_{1g} modes (B_{1g}^1, B_{1g}^2, B_{1g}^3). Note that the B_{1g}^3 peak is weak and manifests as a right shoulder peak near the strong A_g^3 peak in the experimental spectra in Figure 4(a). To further validate the peak symmetry assignments, polarized Raman measurements were then carried out. A_g and B_{1g} modes have dramatically different response behaviors to laser polarization owing to their different Raman tensors in Eq. S3: B_{1g} modes cannot be observed under the parallel configuration $\bar{z}(x,x)z$ (i.e., e_i = e_s = (1, 0, 0)) while A_g modes can; on the other hand, A_g modes cannot be observed under the perpendicular polarization configuration $\bar{z}(x,y)z$ (i.e., e_i = (1, 0, 0) and e_s = (0, 1, 0)) while B_{1g} modes can. Consequently, the switch of the laser polarization configuration enables their differentiation. Similar phenomena have been reported for group-6 TMDs like MoS_2[2, 23] and black phosphorus[20, 24, 25]. As shown in Figure S9 in SI, in both the simulated and experimental polarized Raman spectra of

$PdSe_2$, the three A_g peaks indeed appear under $\bar{z}(x,x)z$ while the three B_{1g} peaks appear under $\bar{z}(x,y)z$. Notably, for the A_g^1-B_{1g}^1 mixed peak in the unpolarized spectra, we are able to separate them under $\bar{z}(x,x)z$ and $\bar{z}(x,y)z$. In addition, the weak B_{1g}^3 peak overshadowed by the strong A_g^3 peak in the unpolarized spectra reveals itself after the A_g^3 disappearance under $\bar{z}(x,y)z$.

The symmetries of *N*-layer (*N*L) $PdSe_2$ films are different from those of the bulk: odd *N*L $PdSe_2$ belongs to space group $P2_1/c$ (No. 14) and point group C_{2h} (2/m); even *N*L $PdSe_2$ belongs to space group $Pca2_1$ (No. 29) and point group C_{2v} (mm2). Strictly speaking, bulk, odd and even *N*L $PdSe_2$ belong to different point groups, and thus their Raman peak symmetry notations can be different. For the six aforementioned Raman modes, from bulk to odd *N*L, A_g peak symmetry remains while B_{1g} is changed to B_g; from bulk to even *N*L, A_g peak symmetry is changed to A_1 while B_{1g} is to B_1. Furthermore, from bulk to *N*L systems, some Raman-inactive modes are activated due to the symmetry reduction, such as the new Raman peaks on the left of the A_g^1-B_{1g}^1 mixed peak in Figure 4(a) and 4(b). The detailed and strict symmetry assignments for all peaks are presented in Figure S8. Here, our focus is on the six characteristic Raman modes originated from the bulk, and for simplicity and consistency, the bulk notations are used for all thicknesses, a common practice in the literature. It is interesting to note that the five peaks (A_g^1-B_{1g}^1, A_g^2, B_{1g}^2, A_g^3, and B_{1g}^3) generally up shift with the thickness reduction from bulk to 1L. In particular, Figure 4(d) shows both the experimental (black) and theoretical (red) frequencies of A_g^1-B_{1g}^1, B_{1g}^2 and A_g^3 peaks at different thicknesses. Although the calculated frequencies are systematically smaller than the experimental ones (by about 9-20 cm^{-1}), the trend of the frequency versus thickness is in agreement: for each peak the frequency generally increases with the decreasing number of layer. For $PdSe_2$, our calculations indicate that the in-plane lattice

constants decrease with the decreasing thickness owing to the reduced interlayer coupling and hybridization. For instance, from bulk to 1L $PdSe_2$, the in-plane lattice a is reduced by ~2%, and b reduced by ~1%. Such lattice shrinking can stiffen the bonds and enhance the restoring forces (we called as the lattice shrinking effect), which is one of the main factors responsible for the upshifts of peak frequencies from bulk to 1L. By fixing the in-plane lattice constants of *N*L systems to the bulk values (i.e., excluding the lattice shrinking effect), the frequencies are systematically lowered by up to 7 cm^{-1} (more details in Table S4). With the lattice shrinking effect excluded, the amplitudes of the frequency shift with the thickness are expectedly smaller, but the computed frequencies of most Raman modes still increase with the decreasing thickness (Table S4). This suggests the presence of other contributing effects. It has been reported that larger force constants are present at the surface of the thin film due to the loss of neighboring layers, which is called the surface effect[26]. Such an effect grows stronger with the decreasing thickness owing to an increasing percentage of surface bonds relative to interior bonds. Consequently, the surface effect could result in the frequency increase of a Raman mode with the decreasing thickness, and it is responsible for the upshift of the characteristic E_{2g}^1 mode with the decreasing thickness in group-6 TMDs like MoS_2 [27-29]. Similarly, the surface effect is also one of the factors accounted for the experimentally observed upshifts of Raman modes in $PdSe_2$. Note that for the A_g^1-B_{1g}^1 mixed peak, its experimental frequency shift as a function of the thickness (black in Figure 4(d)) does not follow a strict monotonic trend. This could arise from the fact that it is the mixture of two peaks. It could also be due to the thickness effect, which has opposite influence on the frequency shift compared to the lattice shrinking effect and surface effect discussed above. According to an intuitive harmonic oscillator model, the frequency of a phonon mode should decrease with the decreasing thickness due to the decreasing restoring force by the

removal of layers, which is called the thickness effect[26-28]. The lattice shrinking effect and the surface effect are competing with the thickness effect in terms of the frequency trend as a function of the thickness, which results in the non-strict monotonous upshifts of Raman modes in $PdSe_2$ in Figure 4(d).

Table S4: Calculated frequencies of the bulk-related Raman modes for 1L, 2L and bulk $PdSe_2$.

Thickness	A_g^1-B_{1g}^1 frequency (cm^{-1})		B_{1g}^2 frequency (cm^{-1})		A_g^3 frequency (cm^{-1})	
	lattice optimized	lattice fixed	lattice optimized	lattice fixed	lattice optimized	lattice fixed
1L	140.59	133.56	208.66	207.22	239.42	235.28
2L	138.36	135.40	207.03	205.66	237.23	234.92
bulk	133.96		204.95		234.26	

Temperature-dependent device characteristics

Strong electron-electron interaction has been suggested as the reason for the metal-insulator transition in low-disordered 2D systems, which arises as the system is quantum confined to two dimensions[30]. The strength of this correlation is characterized by the Wegner-Seitz radius given as:

$$r_s = \frac{n_v}{a_B^* \sqrt{\pi n_{2D}}} = \frac{m^* e^2 n_v}{4\pi\varepsilon\hbar^2 \sqrt{\pi n_{2D}}} \qquad \text{(S4)}$$

where n_v is the number of degenerate valleys in the spectrum, $a_B^* = (4\pi\varepsilon\hbar^2)/(m^*e^2)$ is the effective Bohr radius, with ε being the dielectric constant and m^* is the effective electron mass. For a system in which $r_s << 1$, the scaling theory of localization is valid. However, this is not true when $r_s \gg 1$ which is a characteristic for strongly interacting systems. For monolayer MoS_2[30] and ReS_2[31], $r_s >> 1$, similar to the values obtained for our $PdSe_2$ samples (~ 6.3 for few-layer systems, and ~2.8 for several-layer systems). This value was obtained considering the effective mass of electron m* = 0.28 – 0.52, while dielectric constant, ε 1.7 times that of MoS_2 (~$12.5\varepsilon_0$)[32]. This shows that few-layer $PdSe_2$ have stronger Coulomb interactions. Ioffe–Regel criterion predicts the existence of a MIT when $k_F \cdot l_e$ satisfies the criterion $k_F \cdot l_e \sim 1$, with the Fermi wave vector $k_F = (2\pi n_{2D})^{1/2}$, and mean free path of electrons $l_e = \hbar k_F \sigma / n_{2D} e^2$. According to this criterion, for $k_F \cdot l_e \gg 1$ the phase is metallic whereas for $k_F \cdot l_e \ll 1$, the phase is insulating. For our device, at the crossing point of $V_{bg} = 40$ V (corresponding to $n_{2D} = 1.87 \times 10^{12}$ cm^{-2}), we have $k_F \cdot l_e \sim 4.8$, similar to that in few-layer MoS_2 (~2.84)[33]. For several layer systems, $k_F \cdot l_e$ is less than 1, showing a continuous insulating phase.

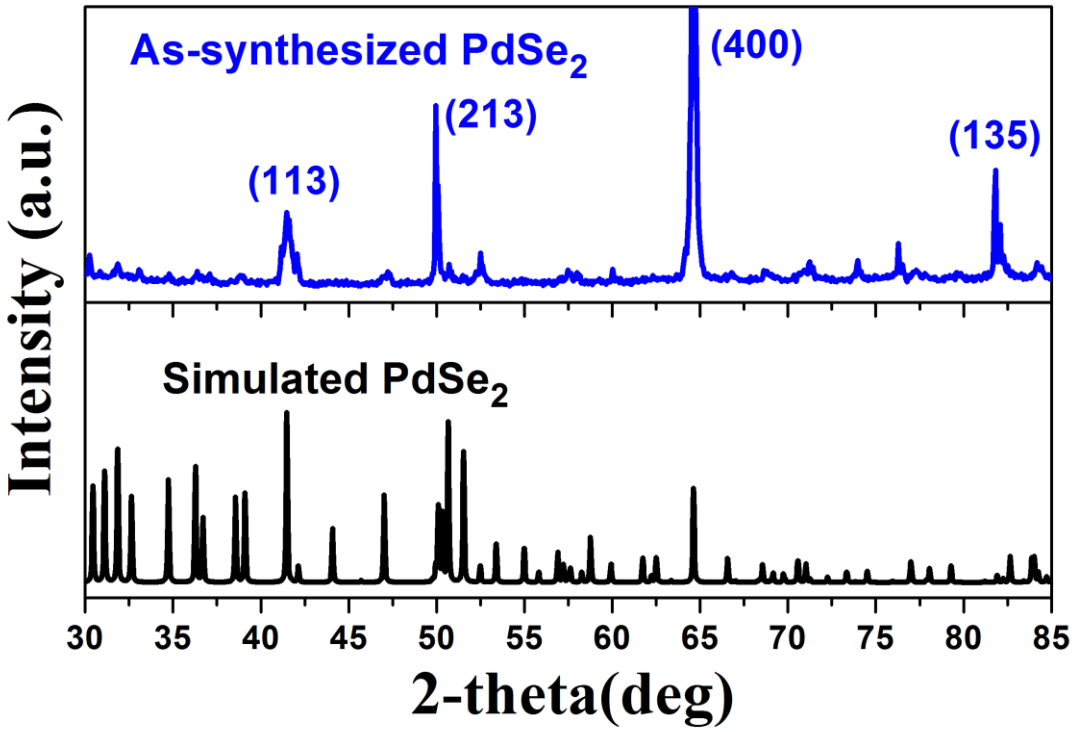

Figure S1: Powder X-ray diffraction (XRD) pattern of as-synthesized $PdSe_2$ (top) compared to simulated XRD pattern (bottom).

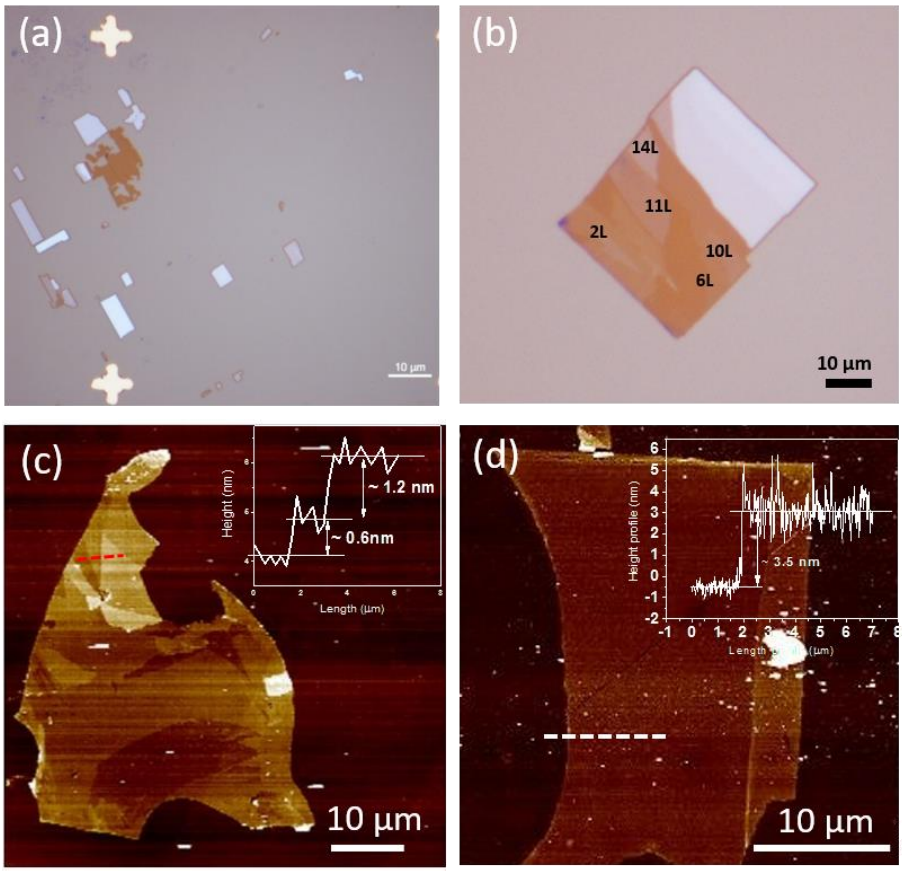

Figure S2. (a-b) Optical images of different number of layers of $PdSe_2$ flakes exfoliated using adhesive tape onto 280 nm thick SiO_2 silicon substrates. The different contrasts correspond to different thicknesses. Most flakes come in regular rectangular shape which makes it easier to identify their crystal-lattice orientation. (c) The AFM image of $PdSe_2$ flake as shown in Figure 1d, Inset shows the line profile scanned from the line in the image. (d) AFM image of monolayer $PdSe_2$ as shown in inset of Figure 1(d) showing ~3.5 nm, and not 0.5 nm, but the Raman spectrum shown in Figure 4(a) indicates the monolayer, which confirms the difficulty to ascertain the very thin thickness of flakes from AFM.

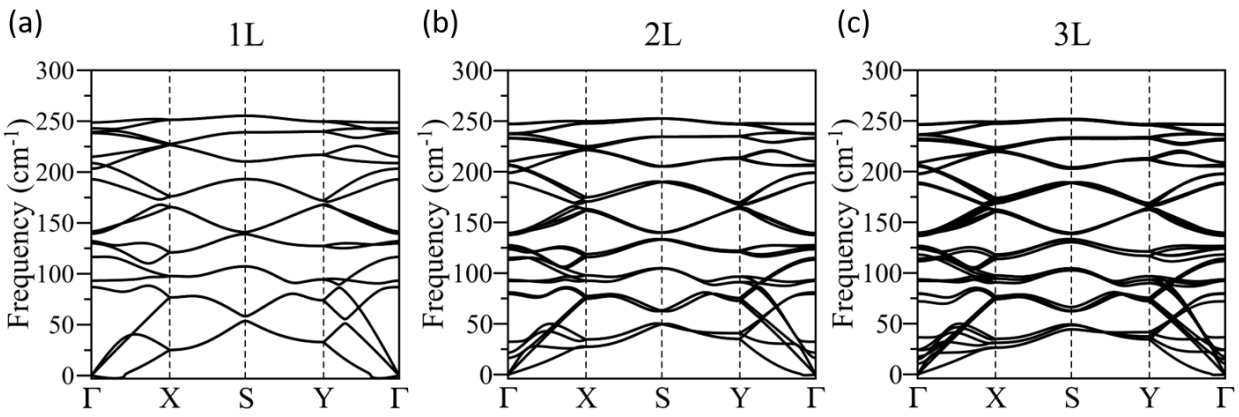

Figure S3. Calculated phonon dispersion spectrum of monolayer and few layer of $PdSe_2$. There are no noticeable soft modes in 1L $PdSe_2$, while the small negative frequencies are probably due to the computational error.

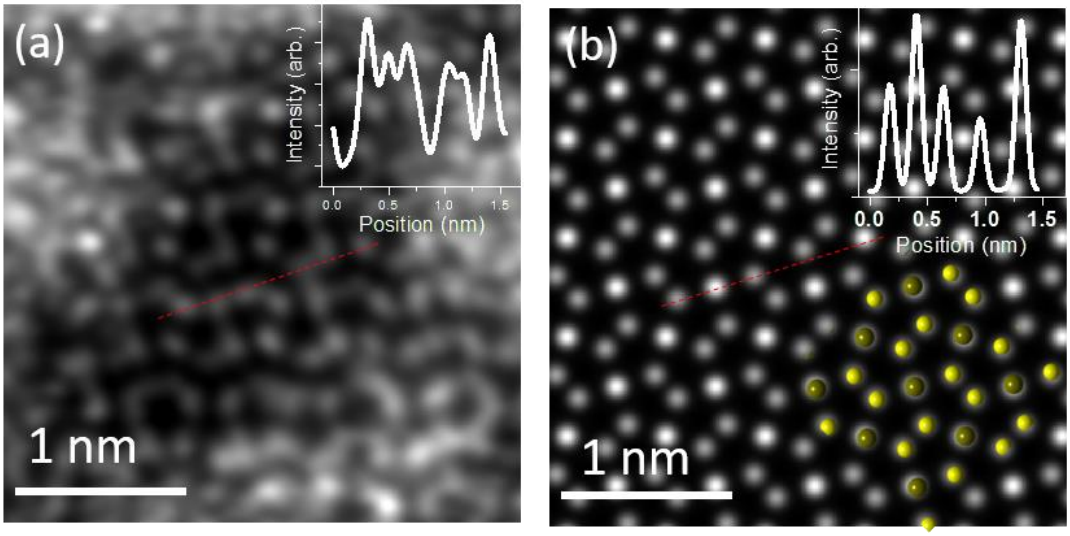

Figure S4. Z-contrast STEM images (a) and corresponding simulated images (b) of monolayer $PdSe_2$. Insets in these images are intensity profiles along the red dashed lines. The ADF intensity in the line profile corresponding to the red dashed line in the inset shows distinct intensity for Pd and Se columns. However, we find that the positions of atomic columns agree with the monolayer model sliced from bulk $PdSe_2$ well while the intensity of the columns does not quite follow the ratio between single Pd and Se atoms. This might be explained by the fact that single-layer $PdSe_2$ might exist on a substrate like SiO_2 but is unstable in the free-standing form or the single-layer $PdSe_2$ could be damaged while transferring on the TEM grid.

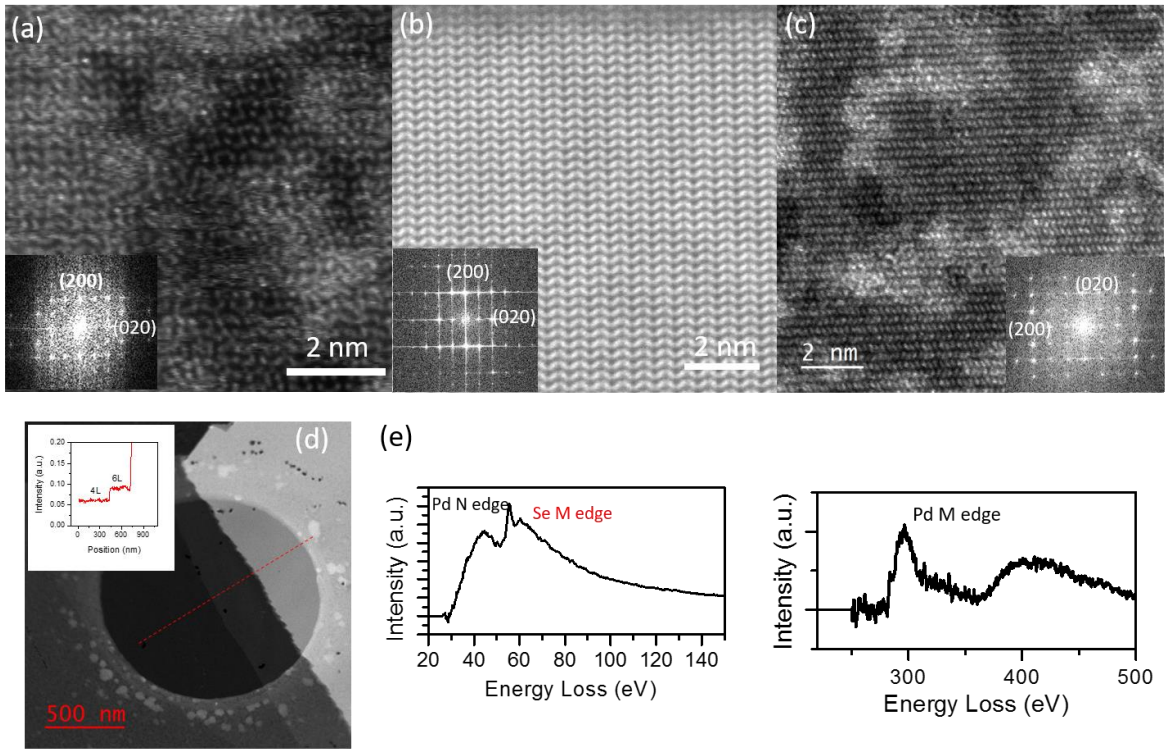

Figure S5. (a-c) The atomic resolution STEM images of $PdSe_2$ monolayer, (b) even layer (c) and odd layer. Insets of these STEM images show the corresponding Fast Fourier Transformation diffraction patterns. Diffraction spots corresponding to two principle planes (020) and (200) are labeled. (d) A low-magnification STEM image of few-layer $PdSe_2$ crystal. Inset shows the line profile of the red dash line in image which the layer thickness is determined to be 4L and 6L according intensity. (e) Electron energy loss spectroscopy of few-layer $PdSe_2$, Pd N edge, Pd M edge and Se M edge are shown in the spectra.

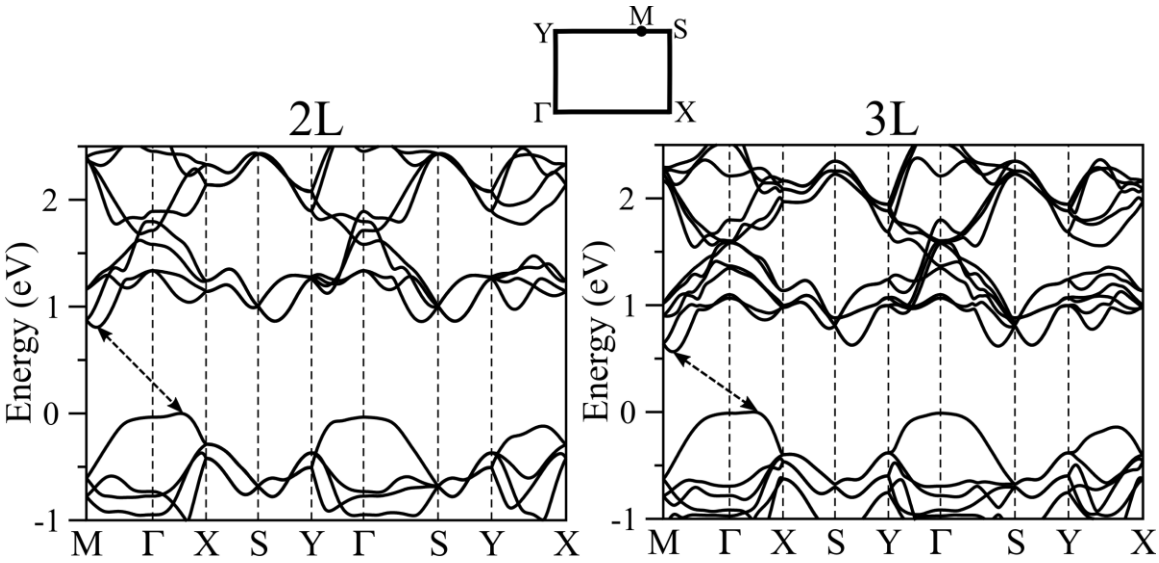

Figure S6. Calculated electronic band structure of 2L and 3L $PdSe_2$ via the optPBE method. The dashed arrows indicate the lowest energy transitions between the valence band maximum (VBM) and conduction band minimum (CBM). The VBM is set at 0 eV. The rectangular shape of the first Brillouin zone is shown on the top.

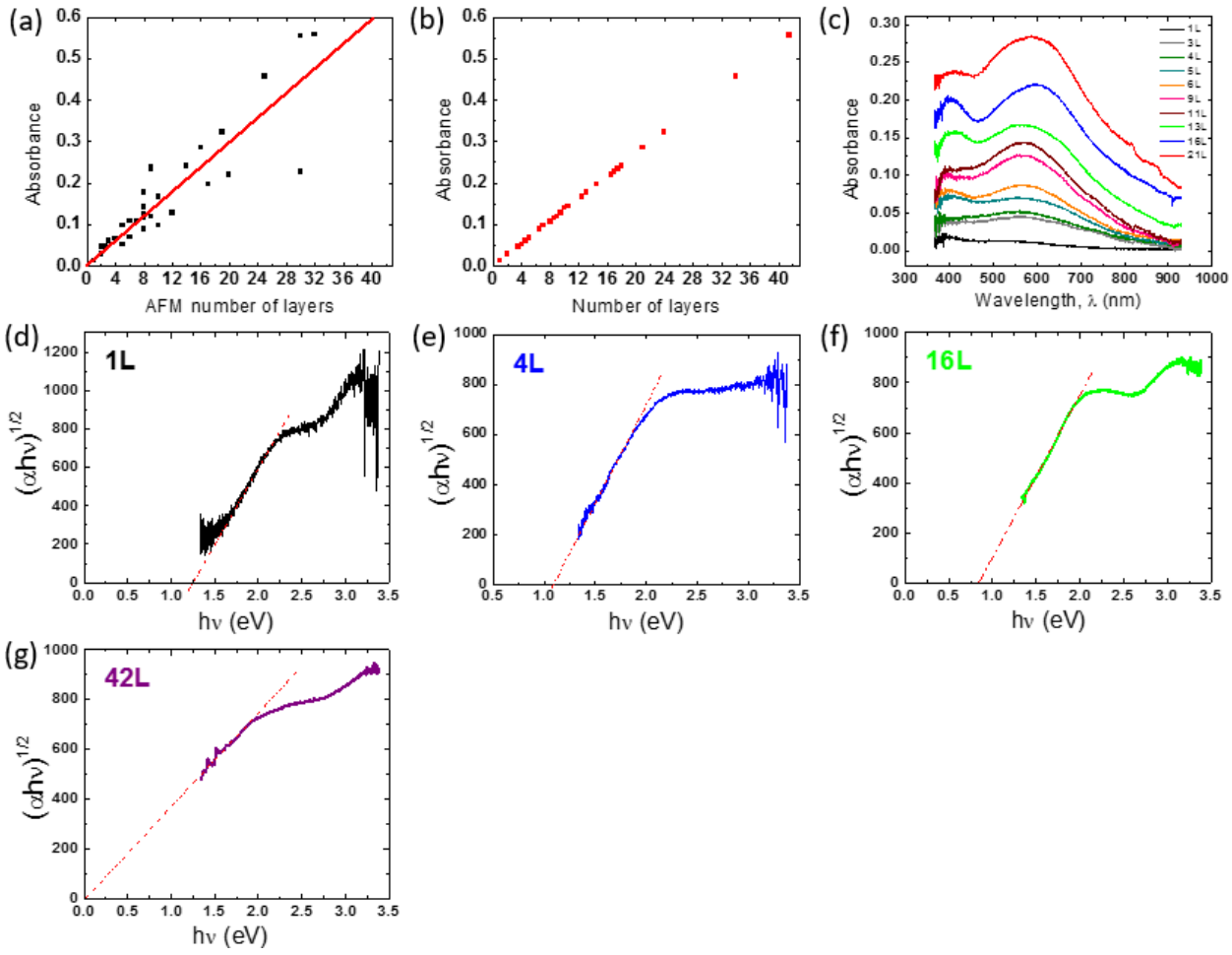

Figure S7. (a) Plot of the absorbance versus the number of layers where the number of layers was determined by AFM. (b) Plot of absorbance with the number of layers determined based on absorbance measured at 800 nm that was used in the analysis of the bandgap. (c) Absorption spectra for the selected number of layers. (d-g) Tauc plots for 1, 4, 16 and 42 layers, respectively which demonstrates how the bandgap was extrapolated.

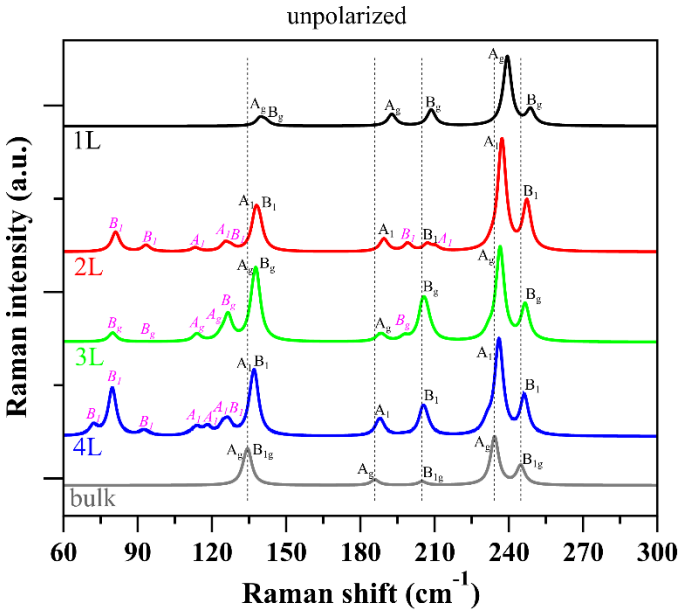

Figure S8. Calculated Raman spectra of $PdSe_2$ via the optPBE method at different thickness. For the six Raman modes in the bulk, in odd *N*L, A_g symmetry remains while B_{1g} is changed to B_g; in even *N*L, A_g symmetry is changed to A_1 while B_{1g} is to B_1. In addition, from bulk to *N*L systems, some Raman-inactive modes are activated due to the symmetry reduction, such as the new Raman peaks on the left of the A_g^1-B_{1g}^1 mixed peak. For peak labeling, the peaks corresponding to those six peaks in the bulk are labeled in black, while new peaks in *N*L systems are labeled in pink italic.

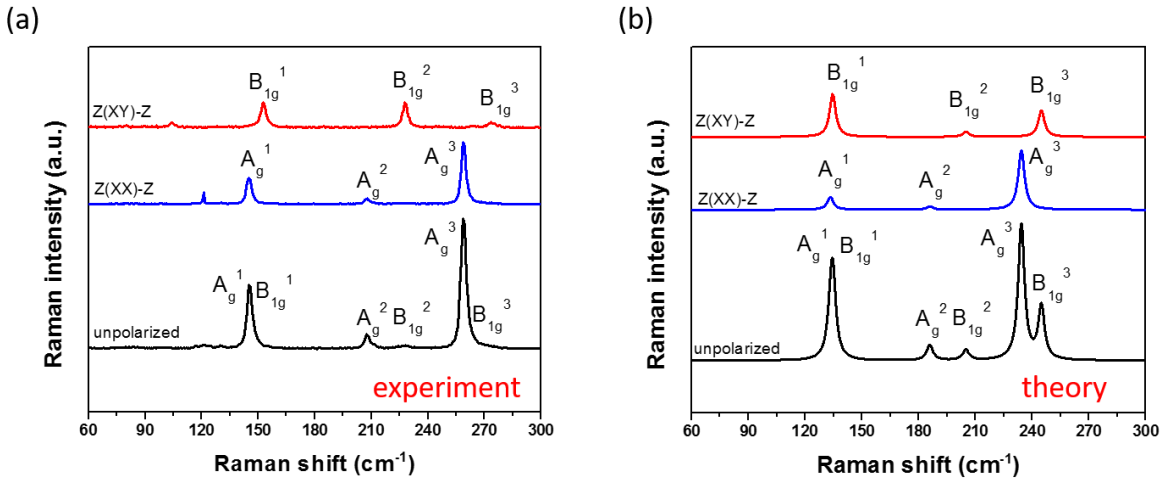

Figure S9. Polarization Raman spectra for (a) several layers (~20 layers) $PdSe_2$ from experiment (b) bulk $PdSe_2$ from theory under different laser polarization configurations: unpolarized, $\bar{z}(x,x)z$, and $\bar{z}(x,y)z$. Both A_g and B_{1g} modes can be observed in the unpolarized spectra, only A_g modes can be observed under the parallel $\bar{z}(x,x)z$ polarization configuration, while only B_{1g} modes can be observed under the perpendicular $\bar{z}(x,y)z$ polarization configuration.

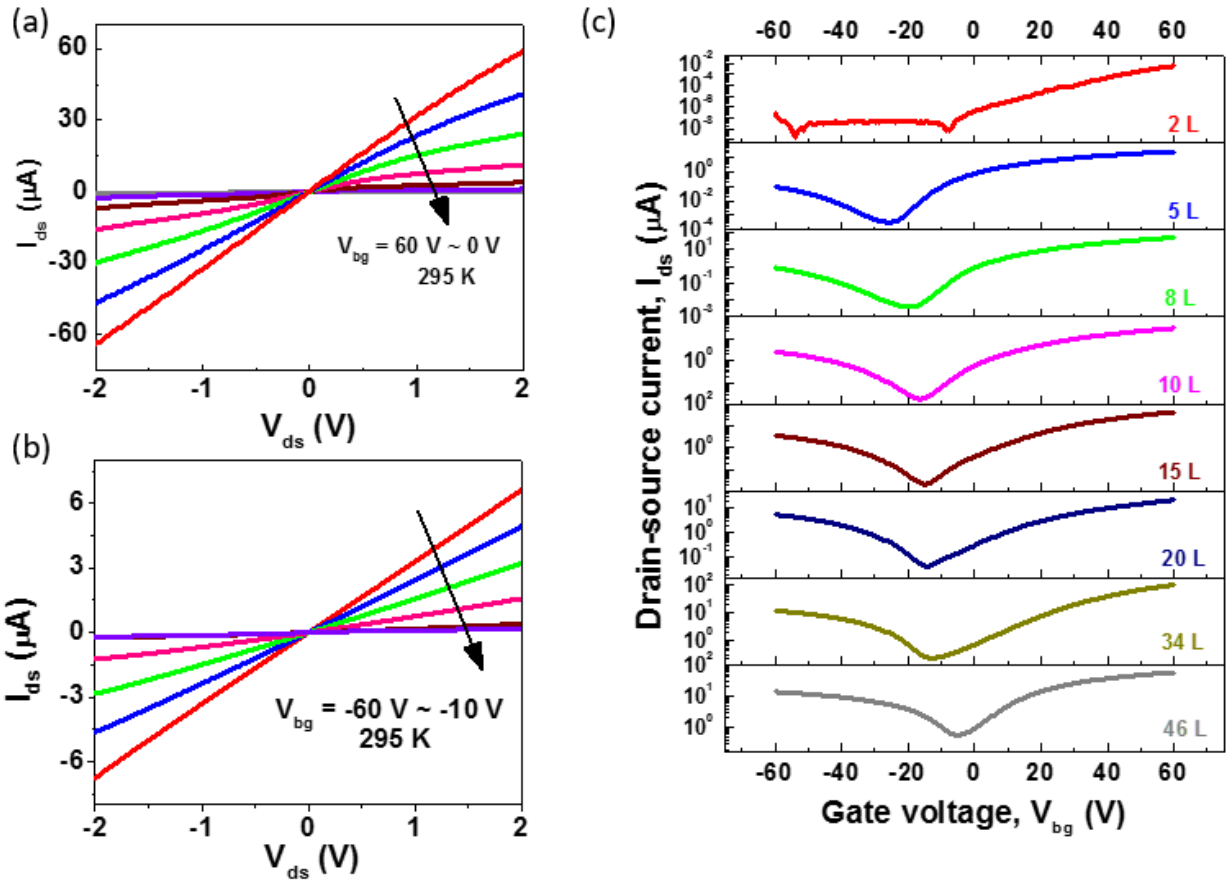

Figure S10. (a-b) Typical output curves showing linear characteristics at 295 K for 20 L at (a) positive back voltages V_{bg} = 60 V ~ 0 V and (b) negative back voltages V_{bg} = -60 V ~ 10 V. (c) Drain-source current versus back gate voltage plot for $PdSe_2$ with different number of layers at V_{ds} = 1.0 V showing ambipolar behavior in all cases at room temperature, with logarithmic plot.

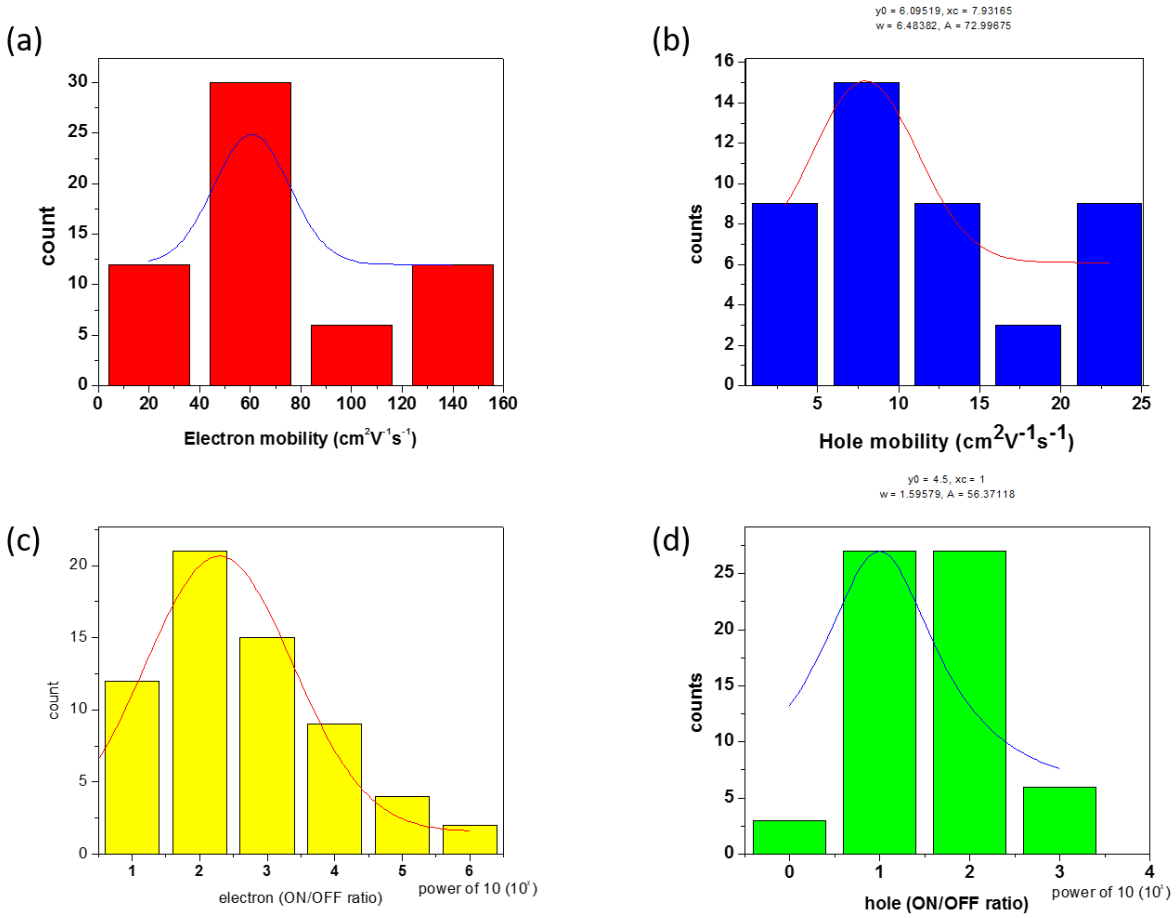

Figure S11. Statistically analysis of the performance of 65 devices based on (a-b) mobility and (c-d) on/off ratio for electron and hole conduction, respectively.

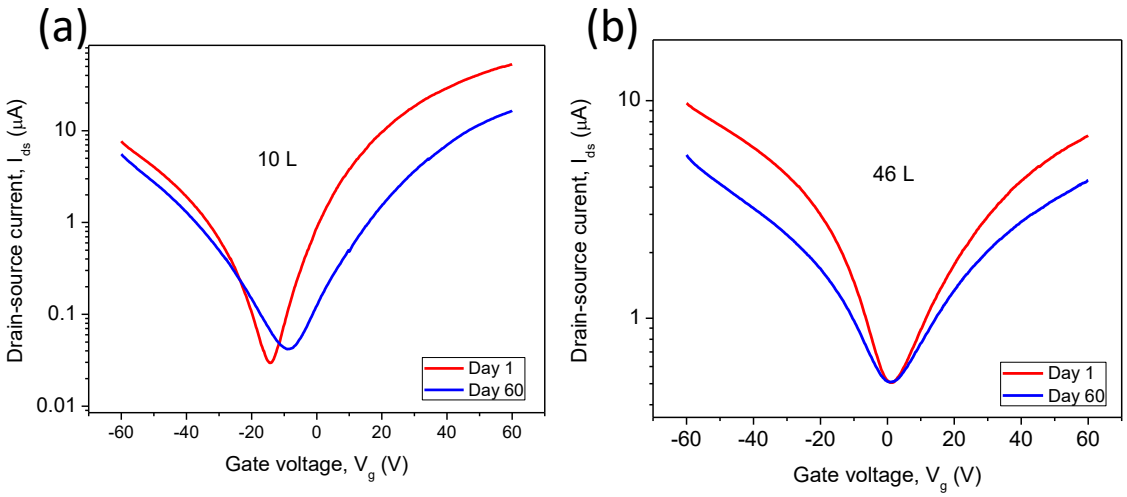

Figure S12. The transfer curve of pristine $PdSe_2$ FET and the device after 60 days exposed in air for (a) 10 L (b) 46 L.

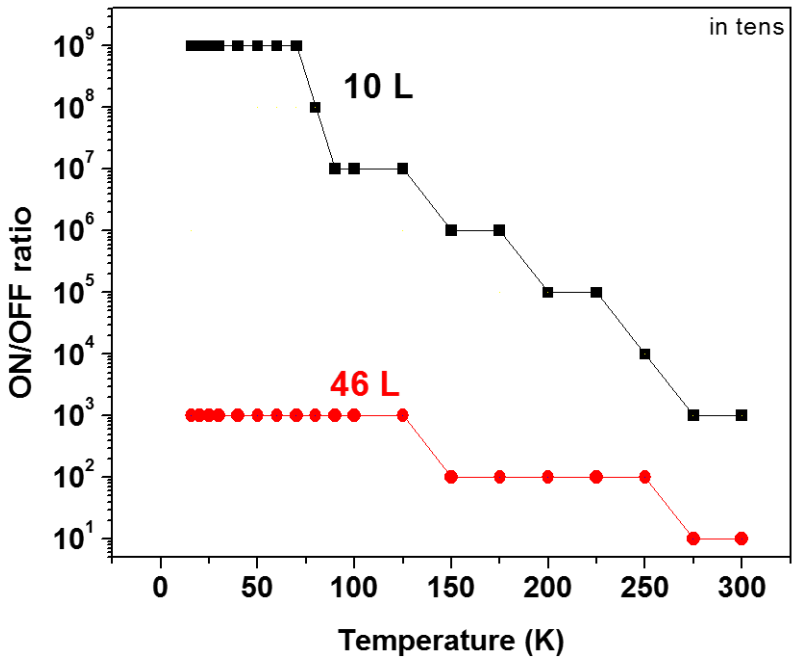

Figure S13. Plot of ON/OFF ratio (rounded to the nearest tens) with temperature for 10 L and 46 L $PdSe_2$.

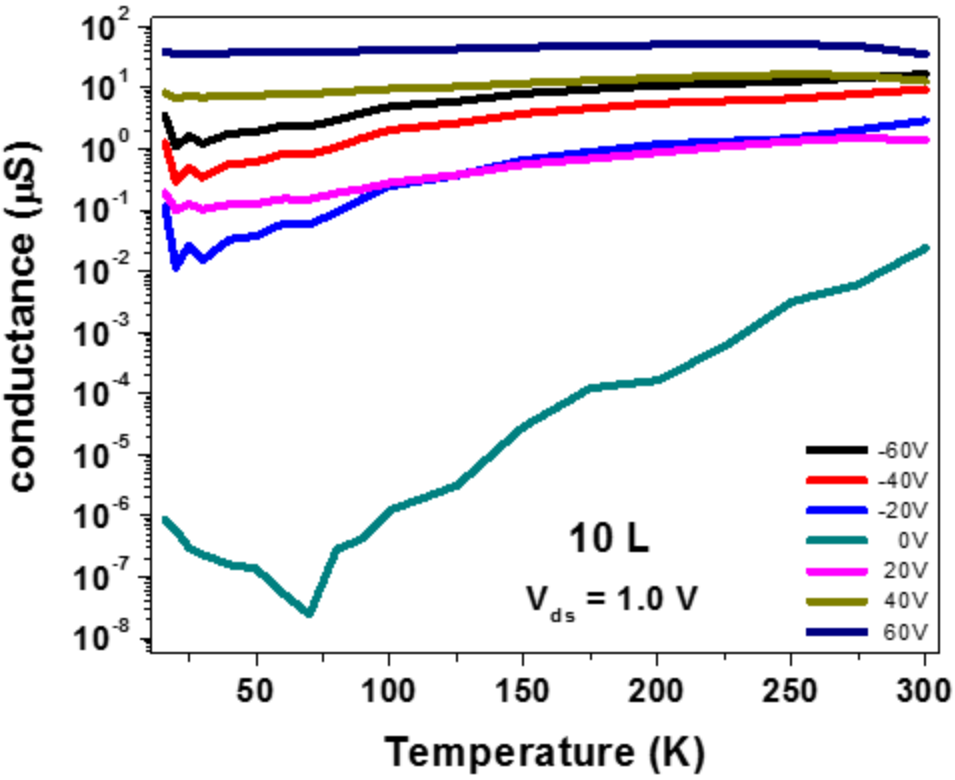

Figure S14. Plot of temperature dependence of the two-terminal conductance at different gate voltages for 10 L device.

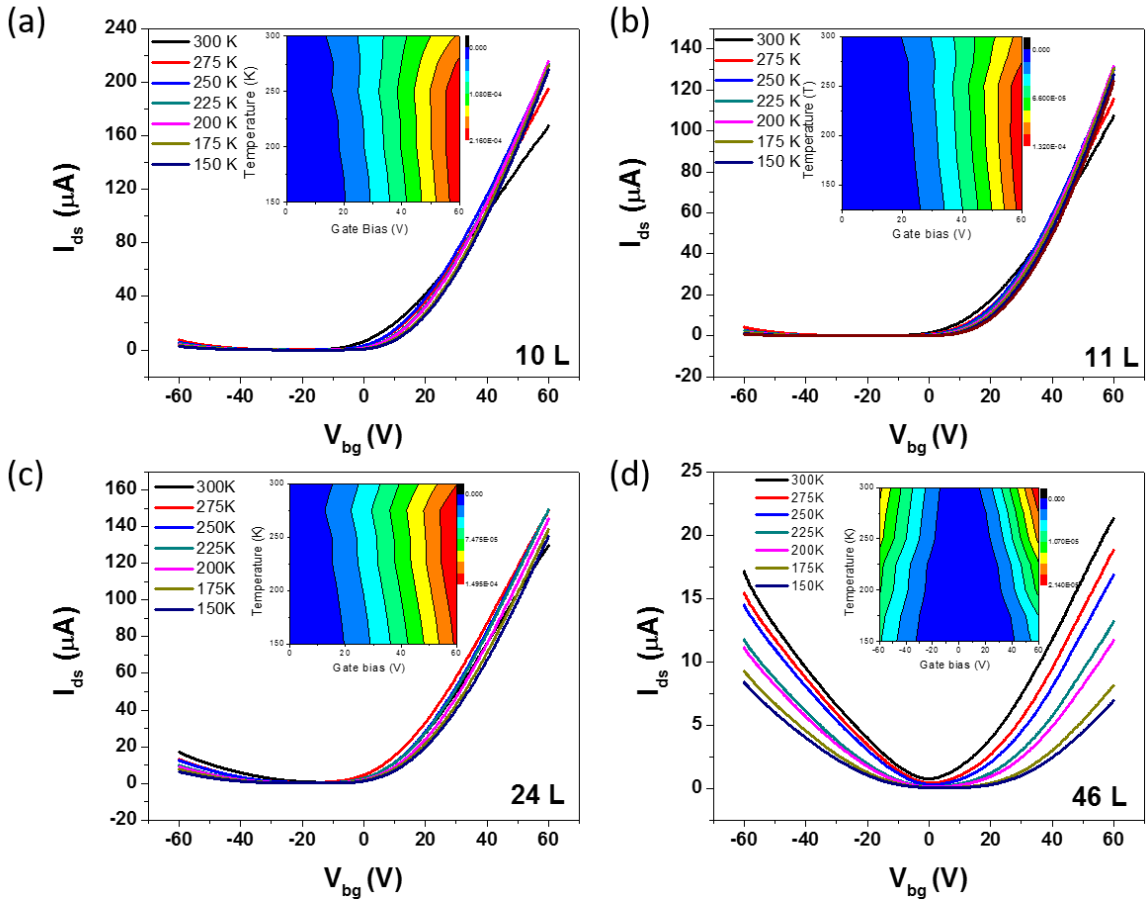

Figure S15. Drain-source current as a function of gate voltage for different temperatures for 10 L (a), 11 L (b), 24 L (c) and 46 L (d) $PdSe_2$ devices, respectively, showing a change in temperature dependence and a crossing at ~40 V for the 10 L and 11 L, and ~50 V for 24 L. Thicker samples shows no crossing. Insets show the corresponding color plots of the conductivity as a function of temperature and gate voltage, which indicate that metal-insulator transition exists for few layers $PdSe_2$, but absent in thick flakes > 24 layers.

References

1. Li, L.; Kim, J.; Jin, C.; Ye, G.; Qiu, D. Y.; da Jornada, F. H.; Shi, Z.; Chen, L.; Zhang, Z.; Yang, F. *Nature Nanotech* **2017**, 12, (1) 21-25.
2. Puretzky, A. A.; Liang, L.; Li, X.; Xiao, K.; Wang, K.; Mahjouri-Samani, M.; Basile, L.; Idrobo, J. C.; Sumpter, B. G.; Meunier, V. *ACS Nano* **2015,** 9, (6), 6333-6342.
3. Iberi, V.; Liang, L.; Ievlev, A. V.; Stanford, M. G.; Lin, M.-W.; Li, X.; Mahjouri-Samani, M.; Jesse, S.; Sumpter, B. G.; Kalinin, S. V. *Scientific Reports* **2016,** 6, 30481.
4. Togo, A.; Tanaka, I. *Scripta Mater.* **2015,** 108, 1-5.
5. Liang, L.; Meunier, V. *Appl. Phys. Lett.* **2013,** 102, (14), 143101.
6. Liang, L.; Meunier, V. *Nanoscale* **2014,** 6, (10), 5394-5401.
7. Umari, P.; Pasquarello, A.; Dal Corso, A. *Phys. Rev. B* **2001,** 63, (9), 094305.
8. Puretzky, A. A.; Liang, L.; Li, X.; Xiao, K.; Sumpter, B. G.; Meunier, V.; Geohegan, D. B. *ACS nano* **2016,** 10, (2), 2736-2744.
9. Gajdoš, M.; Hummer, K.; Kresse, G.; Furthmüller, J.; Bechstedt, F. *Phys. Rev. B* **2006,** 73, (4), 045112.
10. Massote, D. V.; Liang, L.; Kharche, N.; Meunier, V. *Phys. Rev. B* **2016,** 94, (19), 195416.
11. Hulliger, F. *J. Phys.Chem. Sol.* **1965,** 26, (3), 639-645.
12. Wilson, J.; Yoffe, A. *Adv. Phys.* **1969,** 18, (73), 193-335.
13. Sun, J.; Shi, H.; Siegrist, T.; Singh, D. J. *Appl. Phys. Lett.* **2015,** 107, (15), 153902.
14. Soulard, C.; Rocquefelte, X.; Petit, P.-E.; Evain, M.; Jobic, S.; Itie, J.-P.; Munsch, P.; Koo, H.-J.; Whangbo, M.-H. *Inorg. Chem.* **2004,** 43, (6), 1943-1949.
15. Giannozzi, P.; Baroni, S.; Bonini, N.; Calandra, M.; Car, R.; Cavazzoni, C.; Ceresoli, D.; Chiarotti, G. L.; Cococcioni, M.; Dabo, I. *J. Phys. Condens. Matter* **2009,** 21, (39), 395502.
16. Dion, M.; Rydberg, H.; Schröder, E.; Langreth, D. C.; Lundqvist, B. I. *Phys. Rev. Lett.* **2004,** 92, (24), 246401.
17. Cooper, V. R. *Phys. Rev. B* **2010,** 81, (16), 161104.
18. Klimeš, J.; Bowler, D. R.; Michaelides, A. *J. Phys. Condens. Matter* **2009,** 22, (2), 022201.
19. Grimme, S. *J. Compu. Chem.* **2006,** 27, (15), 1787-1799.
20. Ling, X.; Liang, L.; Huang, S.; Puretzky, A. A.; Geohegan, D. B.; Sumpter, B. G.; Kong, J.; Meunier, V.; Dresselhaus, M. S. *Nano Lett.* **2015,** 15, (6), 4080-4088.
21. Aroyo, M.; Perez-Mato, J.; Orobengoa, D.; Tasci, E.; De La Flor, G.; Kirov, A. *Bulg. Chem. Commun* **2011,** 43, (2), 183-197.
22. Denisov, V. N.; Mavrin, B. N.; Podobedov, V. B. *Phys. Rep.* **1987,** 151, (1), 1-92.
23. Zhao, Y.; Luo, X.; Li, H.; Zhang, J.; Araujo, P. T.; Gan, C. K.; Wu, J.; Zhang, H.; Quek, S. Y.; Dresselhaus, M. S. *Nano Lett.* **2013,** 13, (3), 1007-1015.
24. Wu, J.; Mao, N.; Xie, L.; Xu, H.; Zhang, J. *Angew. Chem.* **2015,** 127, (8), 2396-2399.
25. Ribeiro, H. B.; Pimenta, M. A.; de Matos, C. J.; Moreira, R. L.; Rodin, A. S.; Zapata, J. D.; de Souza, E. A.; Castro Neto, A. H. *ACS Nano* **2015,** 9, (4), 4270-4276.
26. Luo, X.; Zhao, Y.; Zhang, J.; Xiong, Q.; Quek, S. Y. *Phys. Rev. B* **2013,** 88, (7), 075320.
27. Lee, C.; Yan, H.; Brus, L. E.; Heinz, T. F.; Hone, J.; Ryu, S. *ACS Nano* **2010,** 4, (5), 2695-2700.
28. Lu, X.; Luo, X.; Zhang, J.; Quek, S. Y.; Xiong, Q. *Nano Research* **2016,** 9, (12), 3559-3597.
29. Zhang, X.; Qiao, X.-F.; Shi, W.; Wu, J.-B.; Jiang, D.-S.; Tan, P.-H. *Chem. Soc. Rev.* **2015,** 44, (9), 2757-2785.
30. Radisavljevic, B.; Kis, A. *Nature Mater.* **2013,** 12, (9), 815-820.

31. Pradhan, N. R.; McCreary, A.; Rhodes, D.; Lu, Z.; Feng, S.; Manousakis, E.; Smirnov, D.; Namburu, R.; Dubey, M.; Hight Walker, A. R. *Nano Lett.* **2015,** 15, (12), 8377-8384.
32. Rasmussen, F. A.; Thygesen, K. S. *J. Phys. Chem. C* **2015,** 119, (23), 13169-13183.
33. Lin, M.-W.; Kravchenko, I. I.; Fowlkes, J.; Li, X.; Puretzky, A. A.; Rouleau, C. M.; Geohegan, D. B.; Xiao, K. *Nanotech.* **2016,** 27, (16), 165203.